Published in final edited form as:
Phys Med Biol. 2010 November 21; 55(22): 6801–6815. doi:10.1088/0031-9155/55/22/013.

Effects of frequency- and direction-dependent elastic materials on linearly elastic MRE image reconstructions

I M Perreard[1], **A J Pattison**[2], **M Doyley**[3], **M D J McGarry**[2], **Z Barani**[4], **E E Van Houten**[4], **J B Weaver**[1,2], and **K D Paulsen**[1,2]

[1]Department of Radiology, Dartmouth-Hitchcock Medical Center, One Medical Center Drive, Lebanon, NH 03756, USA

[2]Thayer School of Engineering, Dartmouth College, 8000 Cummings Hall, Hanover, NH 03755, USA

[3]University of Rochester, 413 Hopeman Engineering Bldg, Rochester, NY 14627, USA

[4]University of Canterbury, Private Bag 4800, Christchurch, 8410, New Zealand

Abstract

The mechanical model commonly used in magnetic resonance elastography (MRE) is linear elasticity. However, soft tissue may exhibit frequency-and direction-dependent (FDD) shear moduli in response to an induced excitation causing a purely linear elastic model to provide an inaccurate image reconstruction of its mechanical properties. The goal of this study was to characterize the effects of reconstructing FDD data using a linear elastic inversion (LEI) algorithm. Linear and FDD phantoms were manufactured and LEI images were obtained from time-harmonic MRE acquisitions with variations in frequency and driving signal amplitude. LEI responses to artificially imposed uniform phase shifts in the displacement data from both purely linear elastic and FDD phantoms were also evaluated. Of the variety of FDD phantoms considered, LEI appeared to tolerate viscoelastic data-model mismatch better than deviations caused by poroelastic and anisotropic mechanical properties in terms of visual image contrast. However, the estimated shear modulus values were substantially incorrect relative to independent mechanical measurements even in the successful viscoelastic cases and the variations in mean values with changes in experimental conditions associated with uniform phase shifts, driving signal frequency and amplitude were unpredictable. Overall, use of LEI to reconstruct data acquired in phantoms with FDD material properties provided biased results under the best conditions and significant artifacts in the worst cases. These findings suggest that the success with which LEI is applied to MRE data in tissue will depend on the underlying mechanical characteristics of the tissues and/or organs systems of clinical interest.

1. Introduction

In vivo characterization of soft tissue mechanical properties offers insight into tissue health and can aid in clinical diagnosis. Magnetic resonance elastography (Muthupillai and Ehman 1996) is a relatively new imaging modality that non-invasively quantifies the elastic property distribution of a tissue or organ system of interest. The MRE technique employed here generates time-harmonic shear waves within tissue and measures the resulting deformations in the dynamic steady-state with a phase-sensitive MR pulse sequence (Weaver *et al* 2001). These displacements are used to produce spatially distributed estimates of tissue stiffness by iteratively solving the inverse elasticity problem (Van Houten *et al* 2001, Van Houten *et al* 1999). Direct inversion methods are also available (Manduca *et al* 2001, Sack *et al* 2008, Sinkus *et al* 2005, 2007, Raghavan and Yagle 1994, Sumi *et al* 1995)

which are attractive computationally. In exchange, the iterative inversion requires more computational effort but has more immunity to the inherent noise in the data.

Under the simplest assumptions, biological tissues behave according to the laws of linear elasticity and various studies have successfully estimated linear elastic mechanical properties *in vivo*, including in breast (Lorenzen *et al* 2002, McKnight *et al* 2002, Van Houten *et al* 2003), brain (Green *et al* 2008, Kruse *et al* 2008), liver (Huwart *et al* 2007, Rouviere *et al* 2006, Yin *et al* 2007), heel fat pads (Weaver, Doyley *et al* 2005) and muscle (Bensamoun *et al* 2006), among other tissues. Nevertheless, many tissues respond differently to induced motion, exhibiting viscoelastic, poroelastic or anisotropic behavior, in which case the purely linear elastic assumption is likely to be a poor approximation. Viscoelastic and anisotropic properties have been observed in breast lesions (Paulsen *et al* 2002, Sinkus *et al* 2005, 2007) and viscoelastic models have been used successfully in MRE studies of brain parenchyma (Cheng and Bilston 2007, Sack *et al* 2008, Weaver, Perrinez *et al* 2005). A recent report (Perriñez *et al* 2009) investigated the effects of using a purely linear elastic model to recover images from experimental data acquired in a poroelastic medium and highlighted the misleading material property distributions that were estimated with the linear elastic approach (Van Houten *et al* 2003).

The goal of this study is to characterize the behavior of linear elastic inversion (LEI) when applied to data recorded from phantom materials with frequency- and direction-dependent (FDD) mechanical properties. Experiments in both linearly elastic and FDD phantoms were conducted over a range of driving signal amplitudes and frequencies and the MRE measurements were reconstructed with LEI to estimate the resulting material stiffness distributions. The purely linear elastic model assumes the displacement field to be real valued (i.e. perfectly in and/or out of phase across the entire phantom)—an assumption that does not hold true when the material is FDD. Results are shown which highlight the limitations of LEI of FDD data. Specifically, LEI produced spatially intact but biased property estimates in FDD phantoms under the best conditions and significant artifacts in the worst cases, the appearance of which (either biased estimates or artifacts) is not easily predicted even in the relatively simple phantom geometries considered.

2. Materials and methods

2.1. Reconstruction algorithm

The reconstruction method employed in this study assumes an isotropic and purely linear elastic response of the phantom to the MRE stimulus in which case its mechanical properties can be characterized by two material parameters known as the Lamé constants. The equation describing the small-scale distortions in an isotropic and linearly elastic material is

$$\nabla \cdot \mu \nabla \mathbf{u} + \nabla(\lambda+\mu)\nabla \cdot \mathbf{u} = \rho \frac{\partial^2 u}{\partial t^2}, \quad (1)$$

where **u** is the displacement vector, ρ is the density of tissue, and μ and λ are the shear and longitudinal modulus, respectively. The Lamé constants, μ and λ, were estimated using a Newton–Raphson iterative scheme based on repetitive solution of (1) with the finite element (FE) method, which we term as LEI throughout this paper as a notational convenience. The computational details of the iterative LEI algorithm have been described elsewhere (Van Houten *et al* 1999, 2001, 2003). Briefly, LEI performs a parameter optimization to find the mechanical property distribution that minimizes the difference between the measured and the computed displacements. The ill-posed nature of LEI is averted by constraining the solution using spatial regularization (Doyley *et al* 2004, Franchois and Pichot 1997, Marquardt 1963). The high computational cost of solving the LEI problem over the entire

domain has been reduced by dividing the region into smaller overlapping zones (Van Houten *et al* 2001) and by parallelizing the code. The influence of zoning parameters (size and overlap) as well as regularization and spatial filtering on the outcome of LEI reconstructions has been investigated (Doyley *et al* 2007). The LEIs reported here were carried out on a Linux cluster with dual-and quad-core AMD opteron nodes.

2.2. Phantoms

A wealth of published data exists on the physical and chemical properties of hydrogels (Al-Ruqaie *et al* 1997, Chatterjee and Bohidar 2005, Doyley *et al* 2005, Gilsenan and Ross-Murphy 2001, Hall *et al* 1997, Higgs and Ross-Murphy 1990, Madsen *et al* 2003, 2005, Sridhar *et al* 2007, Yapp *et al* 2007, Zhang *et al* 2007), but the range of mechanical stiffness values reported is large (e.g. up to two orders of magnitude from less than 1 kPa to more than 100 kPa). The array of material properties listed in a given study depends principally on the type of commercial gelatin (bloom number, animal provenience) and the recipe for making the phantom mixtures. Phantoms are mainly composed of water and gelatin or agar in various proportions. Table salt (NaCl), ethylenediaminetetraacetic acid (EDTA) or formaldehyde is typically added to correct or alter the pH of the solution and to increase the cross linking of collagen strands (extending the shelf life of the phantom and increasing its stiffness). Copper sulfate is often used to produce contrast for MR imaging. The presence and proportion of these additives make the resulting mechanical properties very specific to the particulars of the phantom recipe. It is also worth noting that experimental measurements employ a wide range of techniques: compression tests (Hall *et al* 1997, Hamhaber *et al* 2003, Madsen *et al* 2003, 2005, Sridhar *et al* 2007, Yapp *et al* 2007, Zhang *et al* 2007), indentation (Sridhar *et al* 2007), shear creep (Gilsenan and Ross-Murphy 2001), dynamic oscillation measurements (Al-Ruqaie *et al* 1997, Chatterjee and Bohidar 2005, Doyley *et al* 2003, Higgs and Ross-Murphy 1990, Madsen *et al* 2005, Ringleb *et al* 2005, Yapp *et al* 2007), through-transmission substitutions (Madsen *et al* 2003, 2005), shear wave time-of-flight measurements (Zhang *et al* 2007), and crawling wave estimations (Zhang *et al* 2007) which also contribute to variability in the values reported in the literature.

In this study, various phantoms of 95 × 95 × 40 mm in size were fabricated to exhibit different FDD material properties including viscoelastic, poroelastic and orthotropic characteristics. The composition of each recipe and the materials used in the phantoms are listed in table 1. The linear elastic phantom recipe consisted of porcine skin gelatin (Type A, 300 bloom, Sigma Aldrich) and deionized water (Doyley *et al* 2007) in various proportions for inclusions or background as indicated in table 1.

We used two recipes to create viscoelastic phantoms which exhibited comparable values of the storage modulus but different amounts of loss modulus (see table 5). The first viscoelastic phantom recipe, denoted as viscoelastic (1) in table 1, followed Zhang *et al* (2007) and contained food-based gelatin (Knox), glycerol (Sigma-Aldrich), deionized water and table salt. Its reported loss modulus is below 10% of the storage modulus. The second viscoelastic recipe, listed as viscoelastic (2) in table 2, used porcine skin gelatin (type A, 300 bloom, Sigma Aldrich), glycerol (Sigma Aldrich), EDTA and deionized water (Doyley *et al* 2010) and has a higher percentage of loss modulus (up to 20%). In each phantom, a very small amount of cupric sulfate was added to enhance MR contrast between the inclusions and the background. After manufacture (when necessary, inclusions were formed 24 h before the background), the phantoms were cured at 4 °C for 24 h and warmed to room temperature before testing (for ~3 h).

The phantoms evaluated in this study are described in table 2 for the frequency-dependent materials and in table 3 for the direction-dependent ones.

To evaluate our MRE findings, we obtained independent mechanical measurements of the storage and loss modulus of samples of the gelatin-based phantom materials in table 1 by performing dynamic oscillation tests. These measurements assume an underlying mechanical model (solid viscoelastic material) in order to yield mechanical properties so they might not have led to entirely accurate results for some of the phantom materials used in the study.

2.3. Data acquisition and modeling

A pneumatic actuator was used for inducing motion in the phantom which was placed on the MR table (Philips Achieva 3T) and coupled to an elastic diaphragm as illustrated in figure 1.

Experiments involving the phantoms listed in table 2 were performed with the gelatin block in the position with its widest base in contact with the elastic diaphragm (direction D1 in figure 1(ii)). Complete MRE acquisitions were recorded at three frequencies (75 Hz, 100 Hz, 125 Hz) for three driving signal amplitudes (300, 600 and 900 mV). To investigate directional dependence, the phantoms listed in table 3 were scanned at a frequency of 100 Hz with a driving signal amplitude of 300 mV while oriented in each of three different directions (shown schematically in figure 1(ii)). Direction D1 corresponds to the phantom sitting in the same position as the one used to actuate the table 2 phantoms, while directions D2 (shown in the figure 1(i) photograph) and D3 (rotated vertically 90° from this position) have the phantom sitting with its other two (narrower) bases placed on the diaphragm.

Displacements were measured using a 2D phase contrast spin-echo MR pulse sequence (Weaver *et al* 2001) (TR = 267 ms, TE = 53 ms for 75 Hz, TR = 240 ms, TE = 40 ms for 100 Hz, TR = 192 ms, TE = 32 ms for 125 Hz). The motion-encoding gradients (MEGs) were synchronized with the mechanical excitation and eight different phase offsets were used to characterize the motion. Ten to fifteen slices of 2 mm thickness were acquired with a 64 × 64 in-plane image matrix. The signal-to-noise ratio values for the data sets considered ranged between 30 and 50. Using the motion conversion algorithm described in Wang (2008) and Wang *et al* (2008), continuous phase and amplitude fields were obtained for each individual data set with optional phase unwrapping.

Linear tetrahedral FE meshes (Zhang *et al* 2005) were constructed for each data set. A mesh sensitivity study was conducted which determined that an element size of approximately 0.14 mm (corresponding to meshes with approximately 250 000 elements) was sufficient to obtain modulus estimates that were not influenced by mesh resolution. The displacements were interpolated from the image volume (voxels) onto the mesh nodes and the problem was solved with the LEI algorithm previously described. Each computational run consisted of 100 global iterations, a number which ensured acceptable numerical convergence. Computation of the parallelized LEI reconstruction on eight processors required approximately 5 h of wall clock time.

2.4. Mechanical testing

To obtain independently measured values of the stiffness of the phantom materials evaluated, a dynamic mechanical analyzer (DMA Q-800 TA Instruments)was used. As measuring material stiffness at frequency is not straightforward, the principle of time–temperature superposition (Peters *et al* 1997) was used to retrieve the mechanical properties at frequencies up to 150 Hz, using the Williams–Landel–Ferry equation (Williams *et al* 1955). The mechanical model assumed in the analysis was solid linear viscoelastic and led to values of the storage and loss moduli for each material. Under oscillation, a viscoelastic material presents a dynamic complex modulus defined as the ratio of stress to strain, that can be decomposed into a storage modulus representing the stiffness of the material,

proportional to the energy stored during a loading cycle, and the loss modulus, proportional to the energy dissipated during a loading cycle (Finley *et al* 1989). Cylindrical samples of 5% and 15% elastic gelatin and viscoelastic materials (1) and (2) of 37.3 mm in diameter and height varying between 3.7 and 5.5 mm were manufactured. Before loading in the compression clamp, the samples were lightly coated with mineral oil to prevent water loss and shearing effects at the specimen surface. Frequency sweeps for values between 1 and 20 Hz for a temperature range of 10–20 °C at the same strain rate of 0.3% were conducted. The frequency range was chosen after preliminary testing, such that no resonance effects were encountered, as we found that at frequencies higher than 20 Hz the stress–strain curves were unstable. Five isothermal curves were recorded at temperatures of 10, 12.5, 15, 17.5 and 20 °C respectively, with the 20 °C being the reference temperature. Although we initially considered the 5 °C isothermal curves, we found the data inconsistent, probably due to the high water content of the samples.

3. Results

3.1. Frequency-dependent phantoms: LEI and material testing results

Typical LEIs of the phantoms listed in table 2 are presented in figure 2. The reconstructed stiffness map showed accurate recovery of the location and geometry of the inclusion in the baseline elastic phantom with sharp contrast between the inclusion (15% gelatin) and background (5% gelatin). By contrast, LEI images of phantoms A–D either did not reveal well-defined outlines of the inclusions or inaccurately represented their contrast with the background, except for the linear elastic inclusion in phantom C. In the case of phantom A and the viscoelastic sphere in phantom C (figures 2(ii) and (iv)), the inclusions were not even visible. When the inclusions were clearly evident in the LEI reconstructions, as in phantoms B and D (see figures 2(iii) and (v)) their contrast was estimated inaccurately.

The LEI shear modulus results are shown in table 4 as a function of excitation frequency. The mean shear modulus values were calculated over the geometries occupied by the inclusion and background, respectively, in each phantom. The segmentation was performed on the MR magnitude images and the masks applied to the shear interpolated back to image space. Corresponding standard deviation values are listed. The range of reconstructed values for inclusions and background was large depending on the materials used in each phantom and their volume fraction. In the baseline elastic phantom, an increase in stiffness proportional with frequency and inversely proportional with driving signal amplitude was observed. The reconstructed shear for the 5% gelatin background varied slightly around 4.60 kPa for all the frequencies considered. The estimated mean shear modulus ranged between 11.64 and 13.11 kPa for the 15% gelatin inclusion.

Generally, LEI of the frequency-dependent phantoms exhibited lower values of stiffness at lower frequencies but this trend was reversed in phantoms B and D which showed higher inclusion stiffness at 100 Hz relative to 125 Hz. LEI results in phantom C showed a more consistent trend due to the lower viscoelastic material fraction present. The same viscoelastic material inclusions were recovered with ranges of 2.59–3.73 kPa and 4.71–4.87 kPa in phantoms A and C, respectively. However, the overall stiffness of phantom C was estimated to be higher than that of phantom A presumably because of the higher stiffness of its overall elastic fraction (due to the presence of an elastic inclusion which was stiffer than the background). LEI yielded a range of reconstructed stiffness values from 7.53 to 11.85 kPa for the viscoelastic inclusion in phantom B that was below the values shown in the baseline elastic inclusion which had the same percentage of gelatin but no glycerol or EDTA. LEI reconstruction of the poroelastic inclusion in phantom D exhibited values between 4.89 and 5.80 kPa.

The stiffness of the linearly elastic background (5% gelatin) in all phantoms reconstructed lower or higher depending on the presence of a relatively softer or stiffer inclusion, indicating that the presence of a linearly non-elastic region in the phantom, i.e. the inclusion, can influence the LEI reconstructions in complex and unpredictable ways. For example, in phantom A where the stiffness of the inclusion was low, the background stiffness ranged between 1.91 and 3.25 kPa, whereas in phantoms B and C which had stiffer inclusions the range was 3.89– 4.21 kPa. However, the values reconstructed for the background were even higher at 4.08– 5.06 kPa in phantom D despite the presence of a relatively soft poroelastic inclusion.

Table 5 contains the mechanical properties at a frequency of 100 Hz determined by applying the time temperature superposition principle to the dynamic mechanical measurement data. LEI of the baseline elastic phantom resulted in reconstructed stiffness estimates which show good agreement with the measured storage modulus values, at 100 Hz, for the lower amplitudes. The percentage difference between measured and computed (mean) values was 2% and 14% for the inclusion and background, respectively.

LEI reconstruction of the frequency-dependent phantoms was not as consistent when comparing the imaged and independently measured modulus values. The LEI reconstructed 15% elastic inclusion in phantom C resulted in a percentage difference of 35% relative to the mechanical measurements, which was much higher than the same material inclusion in the baseline phantom. The inclusions in phantoms A and C which were made from viscoelastic (1) material had differences of 25% and 2%, respectively, between the measured and LEI reconstructed stiffness. The reconstructed-measured stiffness percentage difference for the inclusion in phantom B (composed of viscoelastic (2) material) was 82%. Quantitatively, the viscoelastic (2) gel is relatively more viscous, in terms of loss modulus, than viscoelastic gel (1), and the variation between the error values obtained for the two gels when comparing computed and experimentally deduced values supports the fact that the more nonlinearly elastic the material the less accurate LEI proves to be.

A large discrepancy (up to 95%) between the LEI reconstructed data and measured values was also found in the poroelastic inclusion in phantom D for which independent mechanical tests determined the shear modulus to be between 2.0 and 4.0 kPa (Perriñez *et al* 2009).

3.2. Direction-dependent phantom: LEI reconstructions

LEIs of the isotropic and orthotropic phantoms listed in table 2 are presented in figure 3.

The pineapple ring consists of stiffer radial fibers that reinforce an inhomogeneous softer matrix; hence, it was expected to be stiffer than the elastic background, but no mechanical testing was performed to measure its mechanical properties because of the complexity of the material and the uncertainty of the validity of the test results. The mean LEI shear modulus values corresponding to background and inclusions for the two phantoms are listed in table 6.

The mean shear modulus values were calculated over the volumes occupied by the inclusion and background, segment based on the MR magnitude images. LEI images from the isotropic phantom were consistent in terms of the recovered shear stiffness from the three different directions of the applied motion, especially in the background. LEI of the orthotropic phantom resulted in an interesting map of material properties as listed in table 6. The reconstructions found the ring inclusion to be stiffer than the background in two of the three directions (D2, D3) evaluated. When the excitation was applied in direction D1 (perpendicular to the ring), the stiffness of the gelatin core was essentially the same as the pineapple ring.

3.3. Correspondence between model and data

3.3.1. Frequency-dependent data—Introduction of a uniform phase shift of $\pi/4$, $\pi/2$, $3\pi/4$ in the measured motion shows that LEI produced consistent results in the baseline phantom as expected. Panels (i) and (ii) in figure 3 indicate variations in stiffness with phase shift that between 1 and 15% for both the inclusion and background over the range of frequencies and amplitudes considered. Higher vibration signal amplitudes (figure 3, panels (v)–(vi)) resulted in a slightly raised variability in the shear estimates, but the differences were still relatively modest.

By contrast, the frequency-dependent phantoms led to LEIs with much higher percentage differences, up to 50% in the shear modulus reconstructed for various amounts of the phase shift as shown in figure 4. In viscoelastic phantoms A–C and poroelastic phantom D, no trends in the shear curves are apparent. These results indicate that neglecting the relative phase of the motion in the frequency-dependent phantoms when assuming linear elastic behavior does not lead to LEI reconstruction of consistent shear modulus values.

3.3.2. Direction-dependent data—The influence of the direction of actuation on the LEI results for the isotropic and orthotropic phantoms is illustrated in figure 6. LEI reconstructions of the isotropic phantom shear stiffness based on the three actuation directions tested show close values for the elastic inclusion—the relative difference between the results for directions D1 and D2 is 5% and increases to 8% for direction D3. However the values for the background register higher differences: 17% between D1 and D2 and 45% between D1 and D3. Figure 5(i) shows the trends in the mean shear modulus estimates recovered from the three different driving directions.

LEI images of the orthotropic phantom show less consistency with actuation direction highlighting its anisotropy. The inclusion is recovered with increasing stiffness values in directions D1, D2, D3 respectively, with an increase of almost 50% between directions D1 and D3. The background stiffness presents an interesting array of values. The background was divided into two different regions: an inner area corresponding to the core of the pineapple ring and an outer area external to the ring. Although both regions comprise the same (isotropic) elastic material, the LEI reconstructions produced different values in the two regions for each direction with variations of up to 50% as illustrated in figure 5(ii).

4. Discussion

MRE data acquired in phantoms with linearly elastic and FDD mechanical properties were analyzed in order to investigate LEI image reconstruction performance under conditions of data-model match and mis-match. As expected, time-harmonic MRE motion maps recorded in linear elastic phantoms led to LEI images with shear modulus estimates that reflected the values obtained from independent mechanical measurements. The results were stable across variations in frequency and driving signal amplitude and were also largely insensitive to additions of uniform phase shifts in the motion data, consistent with expectations for time-harmonic displacement wave behavior in isotropic, linearly elastic solid materials.

When LEI was applied to data collected from phantoms with FDD mechanical property characteristics, the image results and concomitant shear modulus estimates became more variable and less predictable. While in general the more a phantom material deviated from being linearly elastic the poorer was the LEI performance, simple relationships such as a consistent over-estimation of shear modulus in viscoelastic materials with LEI were not as evident as has been found in other studies (Oudry *et al* 2009). Instead, LEI was observed to be consistently less accurate but in somewhat unpredictable ways that resulted from a complex interplay between multiple factors (e.g. size, shape and contrast of inclusion(s)).

Interestingly, the results reported here were produced under full-developed, steady-state, time-harmonic wave propagation in heterogeneous phantoms which may cause a degree of parameter interplay that did not occur in the Oudry *et al* studies in which plane wave measurements in homogeneous phantoms were evaluated.

The degree of visual degradation in inclusion recovery with LEI in FDD phantoms depended on multiple factors, including the underlying shear modulus contrast, and LEI images appeared to be of lowest quality as the phantom data—LEI model mismatch increased, especially in the poroelastic (phantom D) and anisotropic (phantom E) cases. However, even when the LEI image was visually accurate (e.g. in phantom B), the shear modulus estimates were substantially incorrect and they were certainly less accurate than their counterparts recovered in the linearly elastic phantoms. The strongest evidence of the robustness of LEI in linearly elastic phantoms and the corresponding inconsistency of LEI in FDD phantoms appears in figures 4–6 which report mean shear modulus estimates as a function of added values of uniform phase shift for different frequencies and driving signal amplitudes. Here, variations in the mean shear modulus in both the inclusions and the background were erratic and not as predictable when LEI was applied to phantoms with FDD material properties, suggesting some caution should be exercised when interpreting LEI results in tissues exhibiting these types of mechanical characteristics. In this regard, viscoelastic behavior appears to be tolerated better by LEI in terms of recovering shear modulus contrast relative to poroelastic and anisotropic properties, although the quantitative accuracy of the shear modulus estimates may not be dependable. The overall performance of LEI in FDD phantoms indicates that LEI may be sufficient in certain types of tissue but less effective in others depending on the underlying mechanical composition of the organ system and/or tissues of clinical interest.

5. Conclusions

Data-model match and/or mis-match is an important consideration in the successful deployment of MRE image reconstruction algorithms. In this study, we have applied linear elastic inversion (LEI) to time-harmonic MRE data acquired in phantoms with purely linear elastic as well as frequency- and direction-dependent (FDD) mechanical properties. When the data-model match is consistent, both visual contrast and quantitatively accurate shear modulus values are evident in the images recovered with LEI. LEI images obtained from the data recorded in phantoms with FDD mechanical properties are more variable and less predictable. When sufficient shear modulus contrast exists, visual image contrast is retained in viscoelastic inclusions, although the values estimated are not likely to be accurate. LEI image contrast is less evident in phantoms with poroelastic and anisotropic mechanical properties and the resulting shear modulus estimates are more variable and sensitive to changes in the data acquisition conditions. These findings are important because they suggest that that successful utilization of LEI in tissues is possible but dependent on the specific mechanical property characteristics of the tissues and/or organs systems of clinical interest. Further, even when contrast is observed with LEI in tissue, the underlying shear modulus estimates are not likely to be very accurate. Based on the phantom results reported here, viscoelastic mechanical properties appear to cause less degradation in LEI images relative to poroelastic and anisotropic material property behavior.

References

Al-Ruqaie IM, Kasapis S, Abeysekera R. Structural properties of pectin-gelatin gels: part II. Effect of sucrose/glucose syrup. Carbohydrate Polym. 1997; 34:309–321.

Bensamoun SF, Ringleb SI, Littrell L, Chen Q, Brennan M, Ehman RL, An K-N. Determination of thigh muscle stiffness using magnetic resonance elastography. J. Magn. Reson. Imaging. 2006; 23:242–247. [PubMed: 16374878]

Chatterjee S, Bohidar HB. Effect of cationic size on gelation temperature and properties of gelatin hydrogels. Int. J. Biol. Macromo. 2005; 35:81–88.

Cheng S, Bilston LE. Unconfined compression of white matter. J. Biomech. 2007; 40:117–124. [PubMed: 16376349]

Doyley MM, Feng Q, Weaver JB, Paulsen KD. Performance analysis of steady-state harmonic elastography. Phys. Med. Biol. 2007; 52:2657–2674. [PubMed: 17473343]

Doyley MM, Perreard I, Pattison A, Weaver JB, Paulsen KD. The performance of steady-state harmonic magnetic resonance elastography when applied to viscoelastic materials. Med. Phys. 2010; 37:3970–3980. [PubMed: 20879559]

Doyley MM, Srinivasan S, Pendergrass SA, Wu Z, Ophir J. Comparative evaluation of strain-based and model-based modulus elastography. Ultrasound Med. Biol. 2005; 31:787–802. [PubMed: 15936495]

Doyley MM, Van Houten EE, Weaver JB, Poplack S, Duncan L, Kennedy F, Paulsen KD. Shear modulus estimation using parallelized partial volumetric reconstruction. IEEE Trans. Med. Imaging. 2004; 23:1404–1416. [PubMed: 15554128]

Doyley MM, Weaver JB, Van Houten EE, Kennedy FE, Paulsen KD. Thresholds for detecting and characterizing focal lesions using steady-state MR elastography. Med. Phys. 2003; 30:495–504. [PubMed: 12722801]

Finley, WN.; Lai, JS.; Onaran, K. Creep and Relaxation of Nonlinear Viscoelastic Materials: With an Introduction to Linear Viscoelasticity. New York: Dover; 1989.

Franchois A, Pichot C. Microwave imaging-complex permittivity reconstruction with a Levenberg–Marquardt method. IEEE Trans. Antennas Propag. 1997; 45:203–215.

Gilsenan PM, Ross-Murphy SB. Shear creep of gelatin gels from mammalian and piscine collagens. Int. J. Biol. Macromol. 2001; 29:53–61. [PubMed: 11429189]

Green MA, Bilston LE, Sinkus R. *In vivo* brain viscoelastic properties measured by magnetic resonance elastography. NMR Biomed. 2008; 21:755–764. [PubMed: 18457350]

Hall TJB, Insana MF, Krouskop TA. Phantom materials for elastography. IEEE Trans. Ultrason. Ferroelectr. Freq. Control. 1997; 44:1355–1365.

Hamhaber U, Grieshaber FA, Nagel JH, Klose U. Comparison of quantitative shear wave MR-elastography with mechanical compression tests. Magn. Reson. Med. 2003; 49:71–77. [PubMed: 12509821]

Higgs PG, Ross-Murphy SB. Creep measurements on gelatin gels. Int. J. Biol. Macromol. 1990; 12:233–240. [PubMed: 2096904]

Huwart L, Sempoux C, Salameh N, Jamart J, Annet L, Sinkus R, Peeters F, ter Beek LC, Horsmans Y, Van Beers B. Liver fibrosis: noninvasive assessment with MR elastography versus aspartate aminotransferase-to-platelet ratio index. Radiology. 2007; 245:458–466. [PubMed: 17940304]

Kruse SA, Rose GH, Glaser KJ, Manduca A, Felmlee JP, Jack CR Jr, Ehman RL. Magnetic resonance elastography of the brain. Neuroimage. 2008; 39:231–237. [PubMed: 17913514]

Lorenzen J, Sinkus R, Lorenzen M, Dargatz M, Leussler C, Roschmann P, Adam G. MR elastography of the breast: preliminary clinical results. Rofo. 2002; 174:830–834. [PubMed: 12101471]

Madsen EL, Frank GR, Krouskop TA, Varghese T, Kallel F, Ophir J. Tissue-mimicking oil-in-gelatin dispersions for use in heterogeneous elastography phantoms. Ultrason. Imaging. 2003; 25:17–38. [PubMed: 12747425]

Madsen EL, Hobson MA, Shi H, Varghese T, Frank GR. Tissue-mimicking agar/gelatin materials for use in heterogeneous elastography phantoms. Phys. Med. Biol. 2005; 50:5597. [PubMed: 16306655]

Manduca A, Oliphant TE, Dresner MA, Mahowald JL, Kruse SA, Amromin E, Felmlee JP, Greenleaf JF, Ehman RL. Magnetic resonance elastography: non-invasive mapping of tissue elasticity. Med. Image. Anal. 2001; 5:237–254. [PubMed: 11731304]

Marquardt D. An algorithm for least-squares estimation of nonlinear parameters. SIAM J. Appl. Math. 1963; 11:431–441.

McKnight AL, Kugel JL, Rossman PJ, Manduca A, Hartmann LC, Ehman RL. MR elastography of breast cancer: preliminary results. AJR Am. J. Roentgenol. 2002; 178:1411–1417. [PubMed: 12034608]

Muthupillai R, Ehman RL. Magnetic resonance elastography. Nat. Med. 1996; 2:601–603. [PubMed: 8616724]

Oudry J, Vappou J, Choquet P, Willinger R, Sandrin L, Constantinesco A. Ultrasound-based transient elastography compared to magnetic resonance elastography in soft tissue-mimicking gels. Phys. Med. Biol. 2009; 54:6979–6990. [PubMed: 19887718]

Paulsen KD, Van Houten EE, Doyley MM, Weaver JB. Magnetic resonance elastography in the breast: initial reconstructions of damping coefficient 2002. Proc. IEEE Int. Symp. Biomed. Imaging. 2002:157–160.

Perriñez PR, Kennedy FE, Van Houten EW, Weaver JB, Paulsen KD. Modeling of soft poroelastic tissue in time-harmonic MR elastography. IEEE Trans. Biomed. Eng. 2009; 56:598–608. [PubMed: 19272864]

Peters GW, Meulman JH, Sauren AA. The applicability of the time/temperature superposition principle to brain tissue. Biorheology. 1997; 34:127–138. [PubMed: 9373395]

Raghavan KR, Yagle AE. Forward and inverse problems in elasticity imaging of soft tissues. IEEE Trans. Nucl. Sci. 1994; 41:1639–1648.

Ringleb SI, Chen Q, Lake DS, Manduca A, Ehman RL, An KN. Quantitative shear wave magnetic resonance elastography: comparison to a dynamic shear material test. Magn. Reson. Med. 2005; 53:1197–1201. [PubMed: 15844144]

Rouviere O, Yin M, Dresner MA, Rossman PJ, Burgart LJ, Fidler JL, Ehman RL. MR elastography of the liver: preliminary results. Radiology. 2006; 240:440–448. [PubMed: 16864671]

Sack I, Beierbach B, Hamhaber U, Klatt D, Braun J. Non-invasive measurement of brain viscoelasticity using magnetic resonance elastography. NMR Biomed. 2008; 21:265–271. [PubMed: 17614101]

Sinkus R, Siegmann K, Xydeas T, Tanter M, Claussen C, Fink M. MR elastography of breast lesions: understanding the solid/liquid duality can improve the specificity of contrast-enhanced MR mammography. Magn. Reson. Med. 2007; 58:1135–1144. [PubMed: 17969009]

Sinkus R, Tanter M, Catheline S, Lorenzen J, Kuhl C, Sondermann E, Fink M. Imaging anisotropic and viscous properties of breast tissue by magnetic resonance-elastography. Magn. Reson. Med. 2005; 53:372–387. [PubMed: 15678538]

Sridhar M, Liu J, Insana MF. Elasticity imaging of polymeric media. J. Biomech. Eng. 2007; 129:259–272. [PubMed: 17408331]

Sumi C, Suzuki A, Nakayama K. Estimation of shear modulus distribution in soft tissue from strain distribution. IEEE Trans. BME. 1995; 42:193–202.

Van Houten EE, Doyley MM, Kennedy FE, Weaver JB, Paulsen KD. Initial in vivo experience with steady-state subzone-based MR elastography of the human breast. J. Magn. Reson. Imaging. 2003; 17:72–85. [PubMed: 12500276]

Van Houten EE, Miga MI, Weaver JB, Kennedy FE, Paulsen KD. Three-dimensional subzone-based reconstruction algorithm for MR elastography. Magn. Reson. Med. 2001; 45:827–837. [PubMed: 11323809]

Van Houten EE, Paulsen KD, Miga MI, Kennedy FE, Weaver JB. An overlapping subzone technique for MR-based elastic property reconstruction. Magn. Reson. Med. 1999; 42:779–786. [PubMed: 10502768]

Wang, H. PhD Thesis. Hanover: Dartmouth College; 2008. Optimizing motion encoding and reconstruction in magnetic resonance elastography.

Wang H, Weaver JB, Doyley MM, Kennedy FE, Paulsen KD. Optimized motion estimation for MRE data with reduced motion encodes. Phys. Med. Biol. 2008; 53:2181–2196. [PubMed: 18385527]

Weaver JB, Doyley M, Cheung Y, Kennedy F, Madsen EL, Van Houten EE, Paulsen K. Imaging the shear modulus of the heel fat pads. Clin. Biomech. (Bristol, Avon). 2005; 20:312–319.

Weaver, JB.; Perrinez, PR.; Bergeron, JA.; Kennedy, FE.; Doyley, MM.; Hoopes, PJ.; Paulsen, KD. Proc. ISMRM 2005. Miami, Florida, USA: South Beach; 2005 May 7–13. The effects of interstitial tissue pressure on the elastic shear modulus in MR elastography; p. 618

Weaver JB, Van Houten EE, Miga MI, Kennedy FE, Paulsen KD. Magnetic resonance elastography using 3D gradient echo measurements of steady-state motion. Med. Phys. 2001; 28:1620–1628. [PubMed: 11548931]

Williams ML, Landel RF, Ferry JD. The temperature dependence of relaxation mechanisms in amorphous polymers and other glass-forming liquids. J. Am. Chem. Soc. 1955; 77:3701–3707.

Yapp RD, Kalyanam S, Insana MF. Molecular and structural analysis of viscoelastic properties. Proc SPIE. 2007; 6511:65111Y.

Yin M, Talwalker JA, Glaser KJ, Manduca A, Grimm RC, Rossman PJ, Fidler JL, Ehman RL. A. Assessment of hepatic fibrosis with magnetic resonance elastography 2007. Clin. Gastroenterol. Hepatol. 2007; 5:1207–1213. [PubMed: 17916548]

Zhang JQ, Sullivan JMJ, Ghadyani HA, Meyer DM. MRI guided 3D mesh generation and registration for biological modeling. J. Comp. Inf. Sci. Eng. 2005; 5:283–290.

Zhang M, Castaneda B, Wu Z, Nigwekar P, Joseph JV, Rubens DJ, Parker KJ. Congruence of imaging estimators and mechanical measurements of viscoelastic properties of soft tissues. Ultrasound Med. Biol. 2007; 33:1617–1631. [PubMed: 17604902]

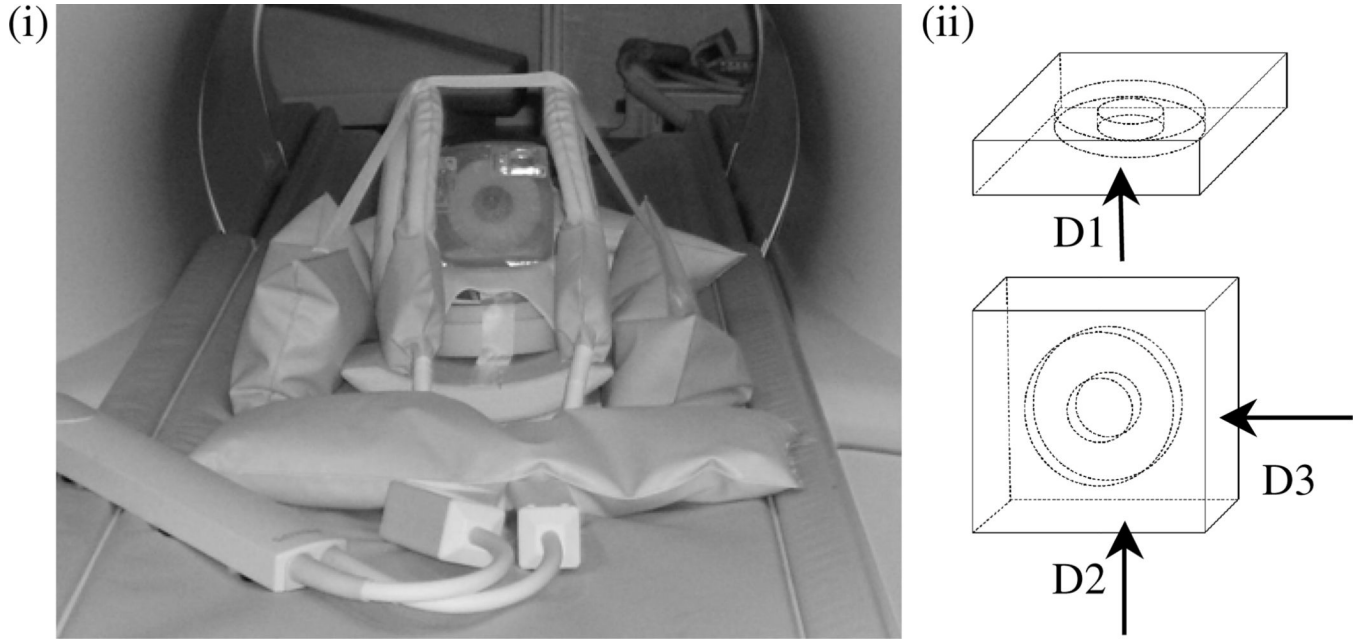

Figure 1.
(i) MRE experimental set-up. Phantom is set in position for acquisition direction, D2, with the inclusion perpendicular to the plane of the elastic diaphragm; (ii) the three orthogonal actuation directions used to evaluate the phantoms in table 3: D1, D2 and D3, respectively.

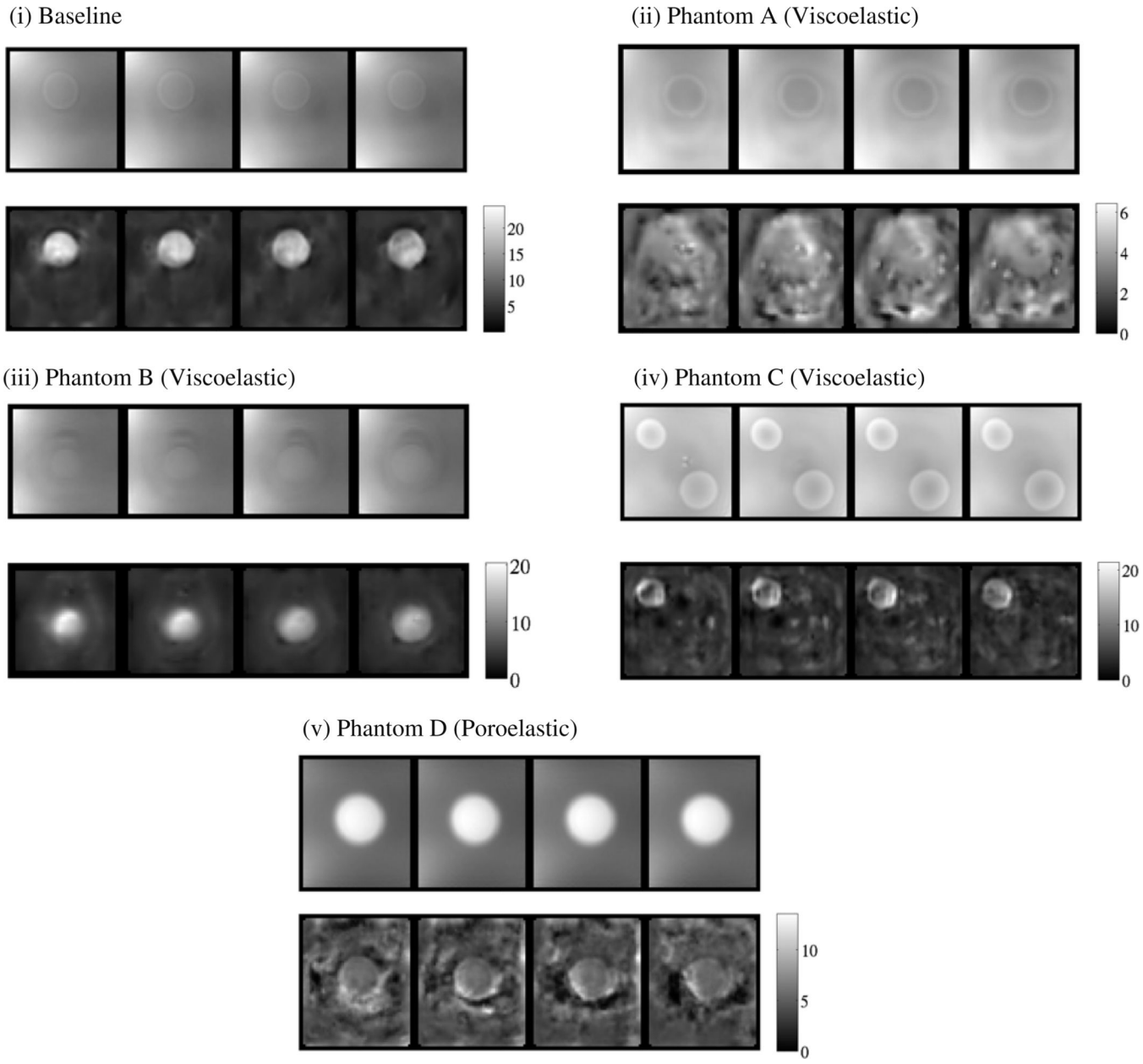

Figure 2.

MR magnitude and LEI images at a frequency of 100 Hz and a driving signal amplitude of 300mV: (i) baseline phantom (elastic), (ii) phantom A (viscoelastic), (iii) phantom B (viscoelastic), (iv) phantom C (viscoelastic), (v) phantom D (poroelastic). Shear modulus scales in kPa.

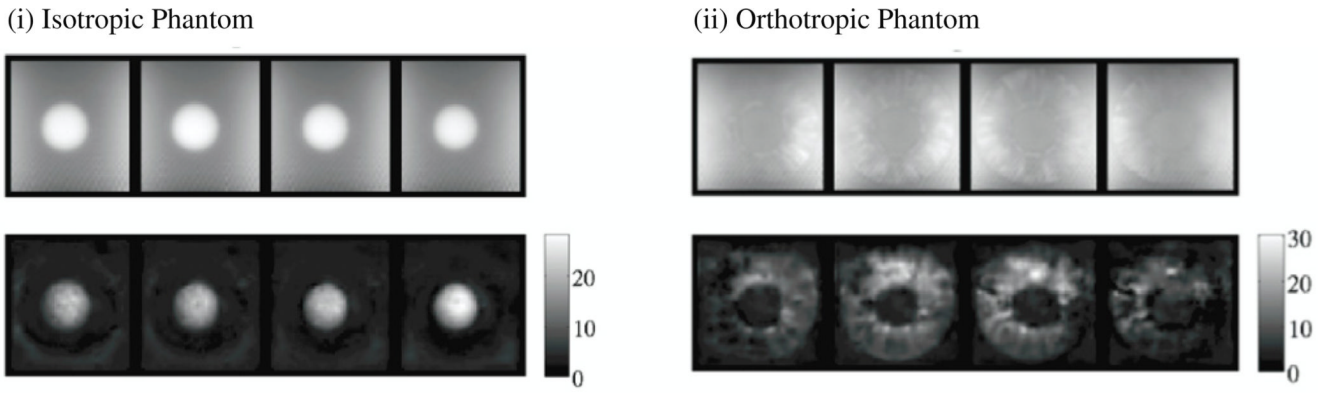

Figure 3.
LEI images of the (i) isotropic and (ii) orthotropic phantoms based on the D3 actuation direction data. Shear modulus scales in kPa.

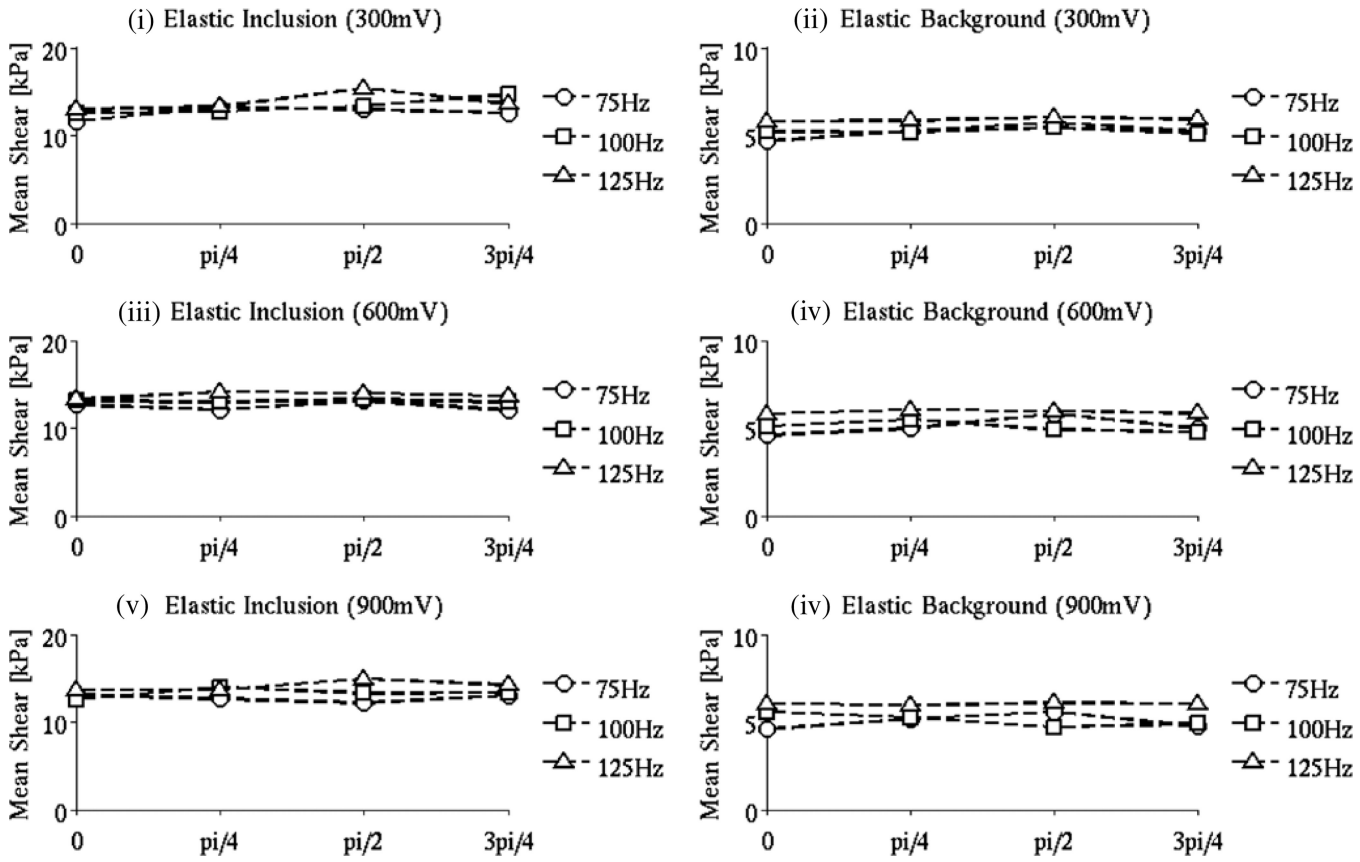

Figure 4.

LEI mean shear modulus values for the background and inclusion (the domains were segmented based on the MR magnitude images) in the baseline phantom as a function of the motion magnitude when a uniform phase shift (0, π/4, π/2, 3π/4) was added. The excitation frequencies considered were 75, 100 and 125 Hz, and the driving signal amplitudes were 300, 600 and 900 mV, respectively.

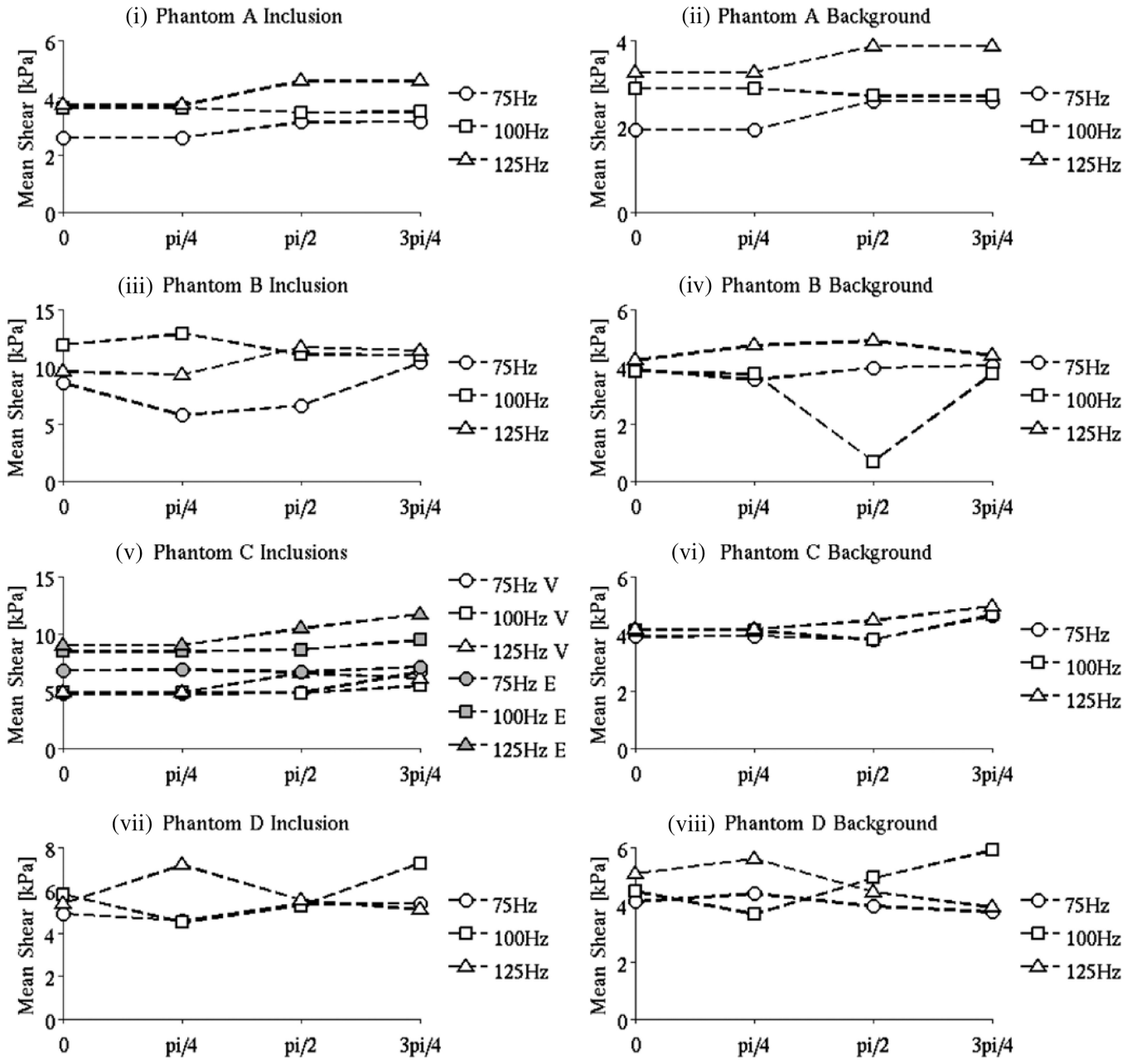

Figure 5.

The influence of introducing a uniform phase shift (0, π/4, π/2, 3π/4) in the measured motion on the LEI shear modulus estimates in phantoms A–D (containing viscoelastic and poroelastic materials). The signal amplitude is 300 mV.

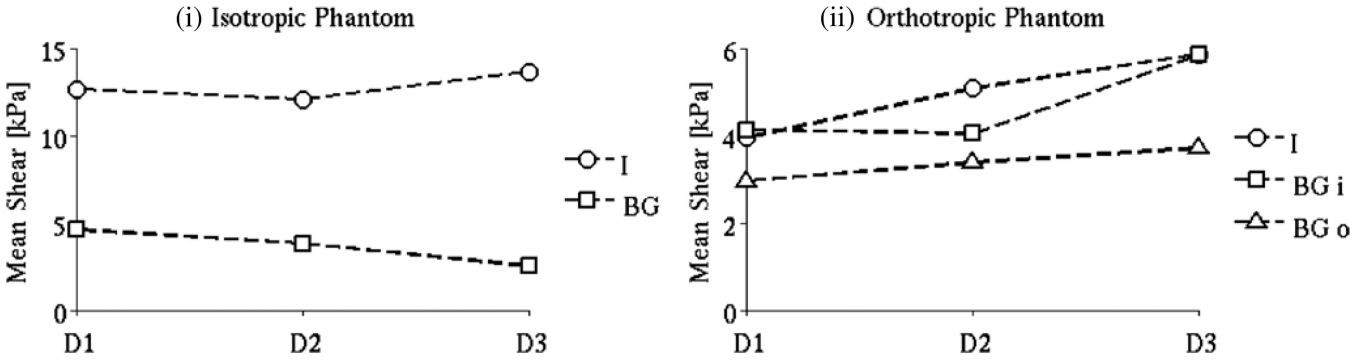

Figure 6.
The influence of the direction of actuation (D1, D2, D3) on the LEI stiffness results for the isotropic and orthotropic phantoms.

Table 1

Phantom material compositions.

Material	Composition
Elastic inclusion (I)	15% porcine gelatin[a]
Elastic background (BG)	5% porcine gelatin
Viscoelastic (1)	7.8% Knox gelatin + 12% glycerol
Viscoelastic (2)	15% porcine gelatin + 20% glycerol + 2% EDTA
Poroelastic	Tofu, Mori-nu firm
Orthotropic	Pineapple ring, Dole canned

[a]% by weight.

Table 2

Description of frequency-dependent phantoms.

Phantom		Materials	Volume fraction (%)
Baseline	BG	Elastic cube (95 × 95 × 40 mm)	94
Elastic	I	Elastic sphere (r = 17.5 mm)	6
Phantom A	BG	Elastic cube (95 × 95 × 40 mm)	94
Viscoelastic	I	Viscoelastic (1) sphere (r = 17.5 mm)	6
Phantom B	BG	Elastic cube (95 × 95 × 40 mm)	94
Viscoelastic	I	Viscoelastic (2) sphere (r = 17.5 mm)	6
Phantom C	BG	Elastic cube (95 × 95 × 40 mm)	93
Viscoelastic	I1	Elastic sphere (r = 9 mm)	1
	I2	Viscoelastic (1) sphere (r = 17.5 mm)	6
Phantom D	BG	Elastic cube (95 × 95 × 40 mm)	93
Poroelastic	I	Poroelastic cylinder (r = 14 mm, h = 40 mm)	7

Table 3

Description of isotropic and directiongroupsy dependent phantoms.

Phantom		Materials	Volume fraction (%)
Baseline	BG	Elastic cube (95 × 95 × 40 mm)	94
Isotropic	I	Elastic sphere (r = 17.5 mm)	6
Phantom E	BG	Elastic cube (95 × 95 × 40 mm)	85
Orthotropic	I	Orthotropic ring (R = 38 mm, r = 18 mm, h = 10 mm)	15

Table 4

LEI shear modulus values from the frequency-dependent phantoms.

		Mean shear stiffness (kPa) at 300 mV amplitude		
Phantom		**75 Hz**	**100 Hz**	**125 Hz**
Baseline	BG	4.67 (SD[a] 1.11)	4.59 (SD 1.12)	4.60 (SD 1.16)
Phantom	I	11.64 (SD 2.65)	12.63 (SD 5.79)	13.11 (SD 4.47)
Phantom A	BG	1.91 (SD 0.81)	2.86 (SD 0.84)	3.25 (SD 0.75)
Viscoelastic	I	2.59 (SD 0.93)	3.62 (SD 0.96)	3.73 (SD 0.95)
Phantom B	BG	3.89 (SD 0.86)	3.84 (SD 0.80)	4.21 (SD 0.75)
Viscoelastic	I	8.53 (SD 1.76)	11.85 (SD 2.14)	9.52 (SD 1.42)
Phantom C	BG	3.89 (SD 1.29)	4.08 (SD 1.50)	4.15 (SD 1.03)
Viscoelastic	I1	6.78 (SD 3.20)	8.41 (SD 3.56)	8.95 (SD 3.04)
	I2	4.71 (SD 1.26)	4.84 (SD 1.22)	4.87 (SD 0.67)
Phantom D	B	4.08 (SD 1.36)	4.44 (SD 1.70)	5.06 (SD 2.27)
Poroelastic	I	4.89 (SD 1.51)	5.80 (SD 2.23)	5.36 (SD 2.40)

[a]SD = standard deviation.

Table 5

Storage and loss moduli values deduced from independent mechanical measurements.

	75 Hz		100 Hz		125 Hz	
Sample	**Storage (kPa)**	**Loss (kPa)**	**Storage (kPa)**	**Loss (kPa)**	**Storage (kPa)**	**Loss (kPa)**
Elastic 5%	3.83 ± 0.34	0.15 ± 0.10	4.01 ± 0.49	0.17 ± 0.16	4.19 ± 0.64	1.86 ± 0.33
Elastic 15%	12.50 ± 2.48	1.28 ± 0.20	12.91 ± 2.34	1.34 ± 0.30	13.15 ± 2.34	1.39 ± 0.40
Viscoelastic (1)	4.92 ± 0.99	0.55 ± 0.15	4.95 ± 0.96	0.54 ± 0.17	5.00 ± 0.92	0.57 ± 0.17
Viscoelastic (2)	5.28 ± 1.76	0.83 ± 0.24	6.50 ± 1.59	1.09 ± 0.27	6.54 ± 1.68	1.13 ± 0.33

Table 6

LEI shear stiffness modulus for the isotropic and direction-dependent phantoms.

		Mean shear stiffness (kPa)		
Phantom		**D1**	**D2**	**D3**
Isotropic phantom	BG	4.59 (SD[a] 1.12)	3.82 (SD 2.06)	2.53 (SD 0.97)
	I	12.63 (SD 5.79)	12.06 (SD 3.38)	13.65 (SD 12.92)
Orthotropic phantom	BG $_i$[b]	4.12 (SD 1.03)	4.04 (SD 1.40)	5.84 (SD 3.01)
	BG $_o$ [b]	2.96 (SD 0.96)	3.38 (SD 1.55)	3.70 (SD 1.82)
	I	3.94 (SD 1.85)	5.07 (SD 2.51)	5.86 (SD 4.11)

[a] SD = standard deviation

[b] i = inner, o = outer background regions relative to the ring shaped inclusion.